Journal of The Electrochemical Society, **153** (4) G283-G290 (2006)
0013-4651/2006/153(4)/G283/8/$20.00 © The Electrochemical Society

Electronic Defect and Contamination Monitoring in Si Wafers Using Spectrally Integrated Photocarrier Radiometry

Derrick Shaughnessy and Andreas Mandelis[z]

Center for Advanced Diffusion-Wave Technologies, Department of Mechanical and Industrial Engineering, University of Toronto, Toronto, Ontario, Canada M5S 3G8

The ability of spectrally integrated room-temperature photocarrier radiometry to image electronic defects and contamination in silicon wafers is presented. Amplitude and phase imaging contrast is a result of signal sensitivity to local variations in the recombination lifetime of photoexcited carriers. Experimental frequency scans are fitted to carrier density-wave theory to simultaneously obtain the recombination lifetime, diffusivity, and surface recombination velocities (front and back). Lifetime measurements are combined with lateral surface scans to produce quantitative lifetime imaging. Contaminated boron-doped silicon wafers with iron concentration $\sim 10^{11}$ cm^{-3} on a baseline of $\sim 5 \times 10^{9}$ cm^{-3} have been successfully imaged and exhibit a much higher spatial resolution than surface photovoltage images. Recombination lifetime measurements before and after photodissociation of FeB pairs have been utilized for quantitative determination of iron concentration; however, lifetime accuracy limitations due to photodissociation by the excitation laser under medium-to-high optical injection levels required for photocarrier radiometric measurements compromise the accuracy of heavy ion (Fe) concentration measurements.
 [DOI: 10.1149/1.2168052]

Manuscript received November 11, 2005. Available electronically February 21, 2006.

Contamination and crystal defects in semiconductor wafers have detrimental effects on silicon device performance and must be closely monitored to maximize yield. A number of characterization techniques are available for the detection of contaminants and defects in crystalline Si wafers. Surface characterization techniques such as Auger electron spectroscopy and X-ray photoelectron spectroscopy can provide information on the relative concentration of specific elements and compounds within approximately 1–10 nm of the sample surface.[1] Characterizing material beyond this depth with these techniques requires sequential measurements following sputtering of surface layers which allows for depth profiling, an approach that is not only destructive but is also time consuming. The depth probed can be significantly increased using an electron microprobe which monitors X-rays emitted from samples that are bombarded by electron-beams.[2] Popular ion-beam characterization techniques include secondary ion mass spectrometry (SIMS) and Rutherford backscattering (RBS).[3] RBS is a nondestructive technique that involves the monitoring of backscattered ions (typically He) that have been projected toward a sample surface with energies of approximately 1–3 MeV. Mass and depth distribution of impurity atoms is available for depths from approximately 100 Å to several micrometers. RBS is limited to detecting heavy atoms in a relatively light substrate and is useful for analyzing surface contamination. In contrast, SIMS involves the sputtering of the sample and the analysis of ejected material in a mass spectrometer (approximately 1% of the sputtered atoms/molecules will be ionized). It allows for the measurement of elemental or molecular composition in the 10^{14}–10^{15} cm^{-3} range but requires knowledge of the matrix (substrate) material to account for variations in secondary ion yield. The applicability of each of the aforementioned techniques for in situ monitoring of contamination and defect generation following particular manufacturing processes is limited by measurement time, vacuum requirements, and the accuracy of quantitative measurements due to variations in yield for the particular physical interaction. A popular instrument for monitoring surface metal contamination is total X-ray fluorescence (TXRF).[4] An X-ray incident at a very shallow angle penetrates nanometers below the sample surface, exciting electrons that release X-rays during deexcitation processes. The energy and intensity of the X-rays can be used to determine the identity and concentration of impurities. The technique is capable of measuring surface densities on the order of 10^{9}–10^{10} cm^{-2}. TXRF is nondestructive and can be used to rapidly determine the concentration of heavy metals such as Cu and Fe but has a relatively poor spatial resolution due to issues of focusing the exciting X-ray beam.

[z] E-mail: mandelis@mie.utoronto.ca

An alternative approach for detecting the presence of contaminants is through their influence on the electronic transport parameters of charge carriers in the semiconductor material. Imperfections in the lattice structure of a semiconductor (for example, the presence of impurities, dislocations, or oxygen precipitates) introduce defect levels into the bandgap that facilitate carrier recombination and compromise carrier recombination lifetime.[5,6] Thus, lifetime measurement techniques can be utilized to monitor the purity of silicon and are well-suited for sensitive contamination control instruments essential for yield improvement.[7] Depth resolution is typically diffusion-limited and thus, the techniques provide the ability to monitor subsurface contamination that may still have detrimental effects on device performance. Lifetime measurement techniques do not, in general, provide information on the particular type of defect but provide rapid, nondestructive identification of nonuniformities in the electrical properties of a wafer that can then be studied using appropriate techniques, if more detailed information on the nature of the contaminant/defect is desired. Of the numerous recombination lifetime measurement techniques,[8] surface photovoltage, which strictly speaking measures diffusion length, has become the most popular for application to contamination monitoring. Specific methodologies involving measurement before and after dissociation of silicon complexes have been developed to uniquely identify and quantitatively measure the concentration of Fe[9,10] and Cu[11] in Si.

More recently, spectrally integrated photoluminescence (PL) has emerged as an industrially viable technique for contamination/defect monitoring of crystalline Si wafers. The spectrum of the radiative emissions from photoexcited silicon has been studied for some time at cryogenic temperatures where low phonon densities make nonradiative processes less dominant over radiative processes, thus improving the radiative yield. There are numerous peaks in the low-temperature spectrum of silicon representing various relaxation mechanisms such as band-to-band recombination, dissociation of excitons, and transitions from band edges to one of the many energy levels introduced into the forbidden energy gap by crystal defects and impurities.[12-15] Despite the large amount of information they can provide, low-temperature photoluminescence measurements are not practical for characterizing whole wafers due to the difficulties associated with maintaining a constant temperature over the entire surface. In addition, the equipment and time required to perform such measurements prohibit use of the technique in-line at a fabrication facility. Of greater interest for industrial applications is the development of room-temperature photoluminescence methodologies. Although the radiative quantum efficiency of silicon at room temperature is extremely low (ca. 2.5×10^{-5} at 300 K[14]), radiative recombination can be detected using efficient collection optics and sensitive detectors. Unlike the low-temperature spectrum, emission

from photoexcited silicon at room temperature is characterized by two energy bands. The first is associated with band-to-band transitions and has a peak at approximately 1.09 eV (1.14 μm).[16] The second band is a broad feature that peaks at approximately 0.73 eV (1.7 μm) and appears for Czochralski (CZ)-grown samples but not magnetic CZ, floatzone (FZ), or epitaxial wafers and is likely due to oxygen-dependent defect complexes.[13,14]

It has been shown that the intensity of the radiative emissions from an excited silicon sample can be related to the recombination lifetime of carriers. Hayamizu et al.[17] showed a direct correlation between the intensity of the band-edge peak and the effective lifetime measured by microwave photoconductivity (μ-PCD), while Kirscht et al.[18] demonstrated a correlation between the integrated radiative intensity and the μ-PCD measured lifetime but make no mention of the spectral content of their photoluminescence signal. Acciarri et al.[19] in turn showed an anticorrelation between measured lifetime and the intensity of the 0.73-eV band from a thermally processed CZ-Si wafer. These results demonstrate the complexity of developing a relationship between radiative intensity and recombination lifetime. For carrier injection levels typically used in optical lifetime measurements, the dominant recombination processes are multiphonon and, at higher injection levels, Auger recombination. These two mechanisms control the overall rate of carrier recombination in the material. Assuming the radiative probability is constant for a given set of samples, a decrease in the nonradiative recombination lifetime, perhaps due to an increase in the defect density or level of contamination, reduces the number of carriers available for radiative recombination and thus lowers the intensity of emitted radiation, as seen in the results of Hayamizu et al.[17] and Kirscht et al.[18] An increase in the density of deep-level radiative recombination centers associated with the 0.73-eV room-temperature band may enhance the radiative emissions in this band, while associated defects may also decrease the nonradiative recombination lifetime, resulting in the relation observed by Acciarri et al.[19] The fact that nonradiative and radiative recombination lifetimes are competing mechanisms and the variations in radiative intensities introduced by the complicated, not well understood, nature of the deep-level radiative recombination centers in silicon makes quantitative lifetime measurement directly from the spectrally integrated intensity of radiative emissions dubious.

Conventional room-temperature photoluminescence (PL) in Si has rarely been reported, perhaps due to the extremely low quantum yield. It invariably involves a nonlinear two-body process of electron-hole band-to-band recombination at high photoexcitation densities in the high-injection regime ($>10^{16}$ cm^{-3}). It is fast ($\sim$2.9 μs decay time[20]) and thus requires considerably high frequencies to be detected under harmonic optical excitation (100 kHz – 10 MHz). The use of both amplitude and phase improves reliability compared to approaches that use a single channel[21] and provides more information than transient decay techniques. Ahrenkiel[22] has also made time-domain lifetime measurements by monitoring the temporal dependence of radiative emissions following pulsed excitation. Krawczyk et al.[23] have proposed a methodology for imaging recombination lifetime using the dependence of the PL signal on injection level. Very recently photocarrier radiometry (PCR)[24] was introduced as a quantitative spectrally gated, modulated PL technique consisting of radiative emissions in a semiconductor. It has been developed through judicious spectral filtering of the thermal infrared component of laser photothermal radiometry (PTR), a mixed infrared PL and nonradiative electronic emission technique.[25] In silicon, at room[24] or higher[26] temperatures, PCR consists of optical excitation responses of the semiconductor, exhibiting a 1.6–2.0 laser power dependence characteristic of band-to-impurity or band-to-defect recombination. Quadratic-range band-edge recombination-induced signals involving electron-hole pairs have also been observed, as expected from two-carrier recombination kinetics.[20,21] Frequency domain PCR has been introduced to study electronic kinetic and recombination phenomena and has yielded signal interpretations in terms of electronic carrier diffusive transport under harmonic excitation,[24] with square-wave optical pulses,[27] and as a lock-in rate-window technique.[27] Due to the high sensitivity of InGaAs photodetectors (the Thorlabs model PDA400 with a built-in preamplifier has a noise equivalent power (NEP) figure of 2.9–8.2 $\times$ 10^{-12} W Hz$^{-1/2}$), PCR is distinct from the aforementioned PL processes[20] due to its ability for low-intensity operation in the subquadratic optical excitation regime. PCR requires much lower frequencies than electron-hole band-to-band recombination and considerably higher signal dynamic range of the detection apparatus. Guidotti et al.[21,28] reported their inability to monitor very weak PL in the low-modulation-frequency ($\sim$kHz), subquadratic regime (where PCR normally operates) and have confined their studies to the quadratic band-to-band recombination regime ($>$10 kHz; mostly $>$100 kHz for highest strength signals). In conclusion, PCR is complementary to band-to-band recombination PL techniques[20,21,28] and thus appears to be significantly more sensitive to band-to-impurity or band-to-defect recombination. PCR can monitor subtler nonlinearities as a function of the power of the optical excitation source, such as near-surface band-bending space-charge-layer processes using an optical bias.[29] The PL imaging technique of Kirscht et al.,[18] although it operates at a fixed modulation frequency, is largely qualitative/empirical and thus the relevant power-law regime is unclear, thus preventing interpretation of the reported signals in terms of quantitative carrier-wave transport processes. Concerning the modulated PCR signal, variations in lifetime are manifested as amplitude changes and phase shifts which allow for imaging of the relative concentrations of electronic defects. In this work the proven ability of PCR to measure carrier lifetime and other relevant transport properties in Si is utilized to demonstrate the suitability of the technique as an electronic defect-imaging tool. The application to quantitative iron concentration measurements in contaminated silicon wafers is also explored.

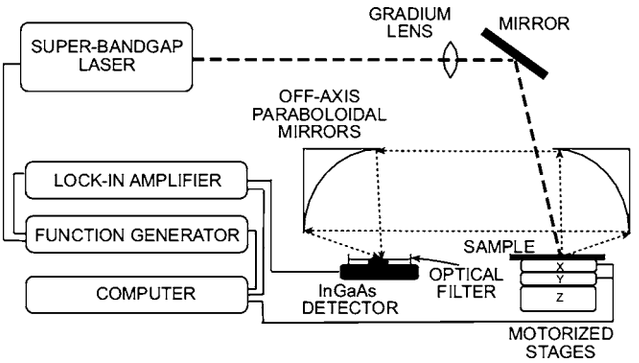

Figure 1. Schematic diagram of experimental system.

Experimental

The photocarrier radiometric system is shown schematically in Fig. 1. An 830-nm diode laser internally modulated using the voltage output from a function generator is used as a carrier excitation source. A gradium lens is used to focus the laser beam onto the sample surface coincident with the focal point of an off-axis paraboloidal mirror that collects a portion of any diffuse backscattered photons. The collected light is then focused onto an InGaAs detector with a switchable gain preamplifier built into the detector housing and a frequency response of up to 10 MHz. The detector has a spectral bandwidth of 800–1750 nm (0.71–1.55 eV) with a peak response at 1550 nm and an active element with a 1-mm diam. The system is designed such that the specular reflection of the excitation beam is not collected by the paraboloidal mirrors and thus is not focused onto the detector. This allows for the collection of near-IR recombination photons from the bulk of the sample and not specularly from the surface. The angle of incidence of the excitation beam is $\sim$28°. A long-pass filter with a steep cut-on and a transmission

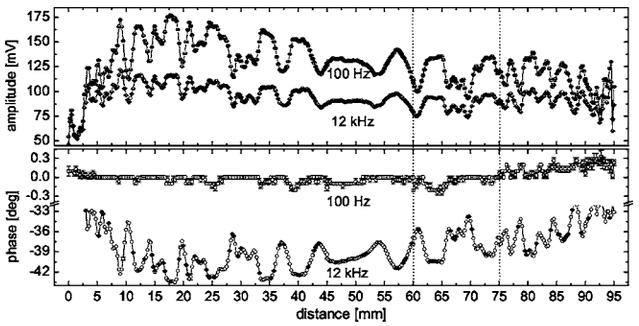

Figure 2. Amplitude and phase from a line scan across the entire length of an n-type Si wafer at modulation frequencies of 100 Hz and 12 kHz.

range of 1042–2198 nm is placed in front of the detector in order to ensure that any diffuse reflections of the excitation source do not contribute to the signal. The signal from the detector is demodulated by a lock-in amplifier. The sample holder is connected to a motorized X-Y stage assembly to allow for sample positioning and imaging, and a third stage in the vertical direction is used to manually adjust the sample to the focal point of the collection optics. All instruments, data acquisition, and lateral sample positioning are controlled using a MATLAB program.

Recombination Lifetime and Depth-Profilometric Subsurface Defect Imaging

PCR line scans performed along the axis of a 100-mm-diam (100) n-type CZ-Si wafer with a 1000-Å thermally grown oxide and a resistivity in the range of 4–12 Ω cm at modulation frequencies of 100 Hz and 12 kHz are presented in Fig. 2. An apparent axis of symmetry at $x \approx 50$ mm suggested the presence of a defect structure with approximately axial symmetry about the center of the wafer. Area surface scans performed at various positions of the wafer confirmed the presence of a ring-like defect pattern. Figure 3 shows the amplitude and phase of one such surface scan performed in the region of 60–75 mm of the line scans of Fig. 2 using a 0.5-mm step size with modulation frequencies of 100 Hz and 12 kHz. It is clearly seen that only the 12-kHz phase image exhibits the ring structure, whereas both high-f and low-f amplitudes exhibit good contrast. These phenomena can be understood in light of Fig. 4: In order to quantify the transport properties in regions of varying PCR signal, line scans were performed in a region of high signal contrast (Fig. 4a and b) using a high-resolution PCR system described in detail elsewhere.[30] The frequency responses of the PCR amplitude and

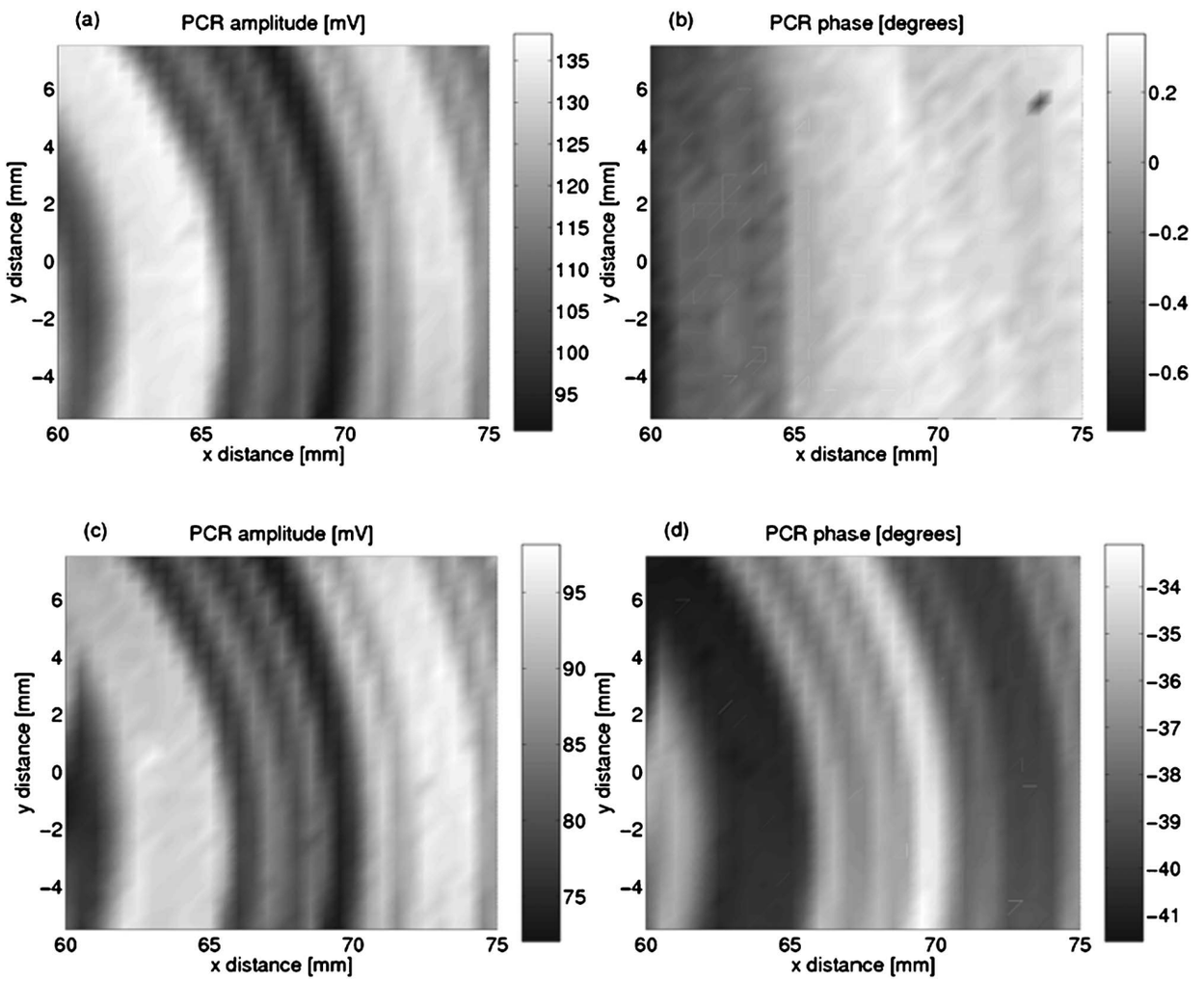

Figure 3. Amplitude (a) and phase (b) images obtained at 100 Hz; and amplitude (c) and phase (d) images obtained at 12 kHz. The line scan of Fig. 2 runs along the line $y = 0$ of the images.

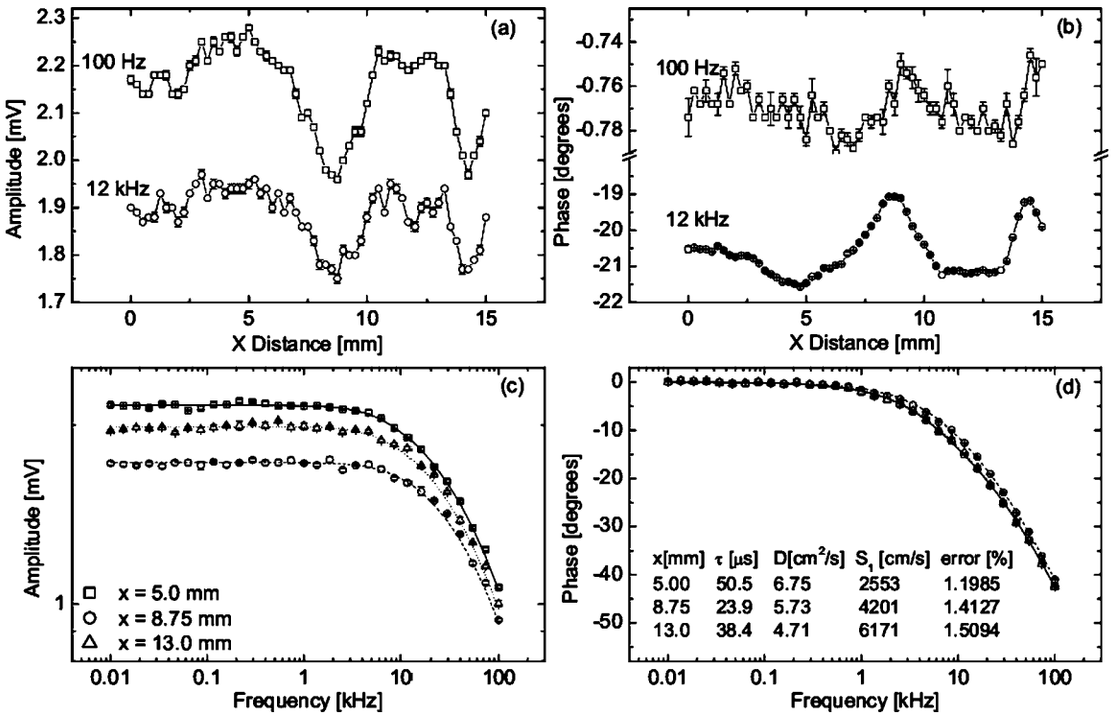

Figure 4. Amplitude (a) and phase (b) line scans of a region of the wafer imaged in Fig. 3a-d, and frequency scan amplitude (c) and phase (d) for three locations along the line $y = 0$. The symbols represent experimental data points and the lines represent the best fits to theory, results of which are shown in the inset at (d).

phase for several locations are shown in Fig. 4c and d, respectively. The symbols represent experimental data points, and the lines represent best fits to the theoretical model presented previously.[24] The electronic transport parameters (recombination lifetime, ambipolar carrier diffusivity, and front surface recombination velocity) extracted from the fits are presented in the inset of Fig. 4d. Simulations showed that the sensitivity to the back surface recombination velocity was low for these transport parameters so it was assumed to be constant at 10^5 cm/s. As expected, the results show a general correlation between the amplitude and phase of the PCR line scans and the effective lifetime resulting from the fit to theory. The injected carrier density averaged over the entire frequency range of interest was calculated to be approximately 10^{18} cm^{-3}. Because the frequency scans of Fig. 4 were performed under these high injection levels, the measured ambipolar diffusivity is found to be much less than the diffusivity of the minority holes, as expected due to bandgap narrowing and carrier–carrier scattering effects.[31] In agreement with the images of Fig. 3, the amplitudes of the line scans and frequency scans of Fig. 4 show approximately constant contrast at all frequencies between 10 Hz and 10 kHz, whereas the phases show little contrast (0.02°) in the 10–500 Hz range. At higher frequencies at which the modulation period becomes commensurate with the lifetime of the sample ($\omega\tau \approx 1$), the phase contrast increases to approximately 2° and is clearly visible in Fig. 3d. Therefore, the modulation frequency range of optimal phase image contrast can be used for a simple determination of the average lifetime and lifetime differences across the region of interest and will thus vary from sample to sample. This is an important characteristic of carrier-density-wave methodologies, compared to dc PL which relies on magnitude contrast: it has previously been suggested that contrast variation with modulation frequency is a result of the frequency dependence of the carrier injection level, which is controlled by the ac carrier diffusion length.[32] While the concentration of carriers relative to the defect density will undoubtedly play a role in altering the carrier recombination dynamics, especially at high injection levels, the present PCR experimental results and simulations strongly suggest that the primary source of contrast with modulation frequency is the relation between the modulation period and the lifetime. This relationship can be physically understood in terms of the primary antinode of a carrier-density standing wave across the thickness of the semiconductor region which exhibits an approximate equality between modulation period and recombination lifetime as a kind of carrier diffusion-wave resonance phenomenon.[33]

While the lifetime cannot be directly extracted from single-frequency images or solely from amplitude images, the optimization of phase contrast from multifrequency images in conjunction with frequency scans at various locations over the surface of the wafer amounts to quantitative lifetime imaging (Fig. 3d and 4d). The time required to fit the frequency scans to the model to obtain transport parameters in addition to the time required to perform sequential point-by-point imaging (approximately 4.5 h for an image comprised of 961 data points) does not allow automated lifetime imaging to be implemented on the current laboratory system. Decreasing the time frame for performing frequency scans through the use of shorter time constants, feasible with the use of more sensitive detectors such as near-infrared photomultipliers and two-dimensional (planar) InGaAs detector arrays using software lock-in amplifiers for parallel signal processing, along with optimization of the fitting algorithm may improve performance to the point where fully automated quantitative lifetime imaging across the sample area becomes practical.

Single lifetime measurements provide a sense of the relative concentration of defects/contamination but generally do not identify the type of defect or nature of the contaminant. Photocarrier radiometry is no different in this respect and identification of the defect/contaminant in Fig. 3 must be deduced using spectroscopic or other ion-specific methodologies. The swirl pattern of the PCR sample images is similar to the well-known circular pattern often associated with the formation of oxygen precipitates,[7] which introduce multiple defect states within the bandgap, predominantly due to the presence of trivalent Si atoms bonded to three Si atoms, leaving a dangling bond[34] acting as efficient recombination centers.[35] Infrared absorp-

tion spectroscopy has been shown capable of distinguishing between oxygen in interstitial and precipitate states.[36] Interstitial oxygen introduces an absorption peak at 1107 cm^{-1} at room temperature (1136 cm^{-1} at low temperatures) that is the result of the antisymmetric stretching of the quasi molecule Si–O–Si. Oxygen precipitates (OPs) introduce multiple absorption bands in the vicinity of the 1107 cm^{-1} interstitial band that must be measured at low temperature to be resolved. At room temperature, OP-related absorption results in a band from approximately 1050 to 1250 cm^{-1} with, generally, absorption at energies less than the interstitial band related to symmetric-shaped precipitates and absorption at energies greater than the interstitial band related to flat precipitate platelets.[36,37] Fourier transform infrared absorption (FTIR) measurements were performed at room temperature on sections of a sample that was processed with the wafer presented above and exhibited similar swirl patterns using a Brüker IFS 66v/S FTIR spectrometer with a Ge/KBr beam splitter and a 4-cm^{-1} resolution. The spectra showed that the regions with lower PCR amplitudes and smaller PCR phase lags, both being indicative of shorter recombination lifetimes, exhibited stronger absorption throughout the OP-related bands as well as at the interstitial related peak of $\sim$1107 cm^{-1}. These independent results confirmed that the features of the presented images in Fig. 3 do indeed represent variations in the relative concentration of oxygen-related electronic defects.

Another useful piece of quantitative information that can be extracted from Fig. 3 and 4 is the effective subsurface depth of the OP. The latter is defined as

$$\langle z \rangle = \frac{\left| \int_0^L z\Delta N(z;\omega)dz \right|}{\left| \int_0^L \Delta N(z;\omega)dz \right|} \simeq \frac{\left| \int_0^L z e^{-\sigma_e z} dz \right|}{\left| \int_0^L e^{-\sigma_e z} dz \right|} \simeq \frac{1}{|\sigma_e(\omega)|} \quad [1]$$

where $\Delta N(z;\omega)$ is the excess free-carrier density due to optical excitation, L is the thickness of the semiconductor sample, and

$$\sigma_e(\omega) = \sqrt{\frac{1 + i\omega\tau}{D^*\tau}} \quad [2]$$

is the complex carrier wavenumber. D^* and τ are the ambipolar diffusion coefficient and the recombination lifetime, respectively. They can both be measured from the frequency scans at the maxima and minima of the swirl pattern, as shown in Fig. 4d (inset). The angular modulation frequency is set at $\omega = \omega_{max}$ at which the maximum striation contrast appears in images such as Fig. 3b and d. The values of $\langle z \rangle$ vary for each position because the electronic transport parameters vary as a function of position, but the approximate values for 100 Hz and 12 kHz in the region of Fig. 3 are 150 and 100 μm, respectively.

Fe Contamination Imaging

Iron in silicon can take the form of an interstitial, form a complex with other atoms, or form a precipitate but does not occupy a substitutional site in moderately doped silicon, as long as vacancies have not been created through ion implantation or irradiation.[38] Iron has a relatively high diffusivity in Si, especially at elevated temperatures, allowing surface contaminants to diffuse into the bulk of a wafer during thermal processing. At high processing temperatures iron occupies an interstitial state, but the high diffusivity allows the iron atoms to travel and form electrically active complexes upon cooling. Interstitial iron is a donor that is positively charged at, or slightly above, room temperature and can form more than 30 complexes with shallow acceptors (such as B, Al, Ga, In, and T1) as well as with gold, silver, zinc, platinum, palladium, sulfur, and oxygen. Approximately 20 energy levels in the bandgap have been attributed to iron and its complexes.[38] In the case of boron-doped p-type Si, the most likely complex formed is with negatively charged boron atoms. Measurements show that Fe-contaminated boron-doped Si wafers possess a shallow donor level at $E_T \approx E_V + 0.10$ eV.[38-40] An acceptor state at ca. $E_C - 0.29$ eV is also associated with the FeB pair and is the dominant recombination center for doping levels between 10^{14} and 10^{16} cm^{-3}.[41] Annealing the sample up to approximately 200°C and cooling to room temperature has been shown to result in a cycling between the concentration of defects at $E_V + 0.4$ eV and $E_V + 0.10$ eV and thus, reproducible transitions between the Fe_i and FeB states[9,42]

$$Fe_i^+ + B^- \rightleftarrows FeB \quad [3]$$

FeB pairs can also be dissociated optically.[40] The use of lifetime measurements before and after FeB dissociation for iron concentration measurements was first implemented using an SPV system along with thermal dissociation.[9] The use of thermal dissociation was quickly replaced by optical dissociation for several reasons, most importantly: (*i*) immersion of samples in a water bath during the quenching process is a potential source of contamination and is not desirable for process wafers; and (*ii*) of the numerous complexes in silicon (such as CrB, B–O, and Cu complexes), fewer are dissociated optically at room temperature than by thermal dissociation, thus reducing the potential for misidentification of contaminants.[10,43] Surface photovoltage instruments that utilize optical dissociation are now well established and are capable of obtaining images with detection limits down to 10^8 cm^{-3}.[44,45] The iron concentration can be written as a function of the recombination lifetime before and after dissociation in a form analogous to that presented by Zoth and Bergholz[9] for diffusion length measurements

$$[Fe] = C(\tau_1^{-1} - \tau_0^{-1}) \quad [4]$$

where the subscripts 0 and 1 denote the state of the semiconductor before and after the dissociation process, respectively, and C is a constant that depends on the density and efficiency of the recombination centers and on the carrier density in the wafer. Assuming the recombination lifetime can be expressed using the classical single-level Shockley–Read–Hall (SRH) theory,[5,6] the value of C for a p-type wafer can be determined from the expression

$$C^{-1} = (N_A + \Delta n)\upsilon_{th}\left[\frac{\sigma_n^{Fe_i}\sigma_p^{Fe}}{\sigma_p^{Fe}(N_A + p_1^{Fe_i} + \Delta n) + \sigma_n^{Fe_i}(n_1^{Fe_i} + \Delta n)} - \frac{\sigma_n^{FeB}\sigma_p^{FeB}}{\sigma_p^{FeB}(N_A + p_1^{FeB} + \Delta n) + \sigma_n^{FeB}(n_1^{FeB} + \Delta n)} \right] \quad [5]$$

where σ is the capture cross section of the assumed single Fe_i energy level, Δn is the injected carrier density, and the superscripts denote association with either the interstitial defect level or that of the FeB pair. Although, strictly speaking, a recombination model accounting for multiple interacting defect levels[46] should be used due to the multiple energy states introduced by the FeB defect, it has been shown that for the resistivity range considered in this investigation (8–12 Ω cm) the acceptor level is the dominant recombination center.[41] The lifetime comparison approach of Eq. 4 is well established for iron concentration measurements in silicon using SPV[44,45] and has also been used with μ-PCD measurements.[47] Published values for the capture cross sections vary significantly.[38,41,48] The results of Macdonald et al.[48] have been used in this work to calculate the value of the prefactor C.

A 150-mm p-type boron-doped industrial CZ-Si wafer with a resistivity of 8–12 Ω cm ($N_A \approx 10^{15}$ cm^{-3}) and a 240-Å thermally grown oxide was obtained, and the iron concentration was measured using a commercial SPV instrument. The SPV measurements showed that the wafer had a relatively uniform iron concentration of ca. 5×10^9 cm^{-3} with several isolated regions with $[Fe] \approx 10^{11}$ cm^{-3}. The PCR imaging results of one such contaminated region, which appeared to be a circular region with a diameter of $\sim$10 mm on the SPV image, region A of Fig. 5, are shown in Fig. 6. The highly resolved PCR images show that the defect is actually a cluster of smaller contaminated regions rather than a single contaminated region, as suggested by the SPV images. The PCR amplitude

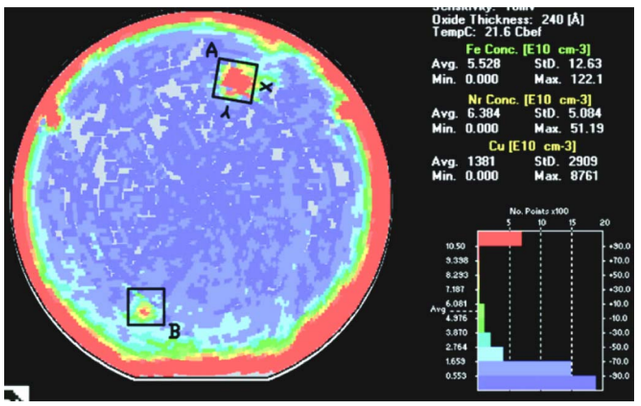

Figure 5. SPV image of the iron-contaminated p-Si wafer (color online).

and phase contrast are well above the noise level for the given iron concentration and demonstrate the ability to monitor iron in silicon at concentrations at least on the order of 10^{11} cm^{-3}. The ultimate detection limit and sensitivity of PCR for iron monitoring has yet to be determined but will require a controlled set of intentionally contaminated wafers with known concentration levels. Evident in Fig. 6 is the evolution of the imaging contrast of an electronic defect with modulation frequency as discussed in the previous section. It is clear that the modulation frequency must be adjusted to optimize the imaging contrast for wafers and/or regions with differing recombination lifetimes. An estimate of the subsurface location of the contaminated region can be obtained from the determination of the mean transport free-carrier properties inside the region and calculation of $\langle z \rangle$ as in Eq. 1.

The differences in defect distributions of Fig. 5 and 6 are a result of the different resolutions of the two instruments. The SPV probe is approximately 6 mm in diameter and severely restricts the imaging resolution. The resolution of photocarrier radiometry, like other techniques relying on laser-induced carrier injection, is laser-beam-size or ac-diffusion-length limited, whichever is larger at a fixed frequency. The ac diffusion length is given as the inverse of the magnitude of the carrier wave number

$$L_{ac} = \frac{1}{|\sigma_e(\omega)|} = \sqrt{\frac{\tau D^*}{\sqrt{1 + \omega^2\tau^2}}} \qquad [6]$$

and is thus a function of recombination lifetime, τ, the ambipolar carrier diffusion coefficient, D^*, and the modulation frequency, ω, of the generation source. Operating at high modulation frequencies can significantly decrease the volume of material sampled by the injected carriers and thus improve lateral resolution of the instrument. The features visible in Fig. 6 (and all other PCR images) appear larger than the actual size of the defect due to resolution limits imposed by the finite beam size and/or carrier diffusion.[26]

The sensitivity to iron defects and the established ability to image lifetime-dependent defects can, in principle, be combined with the quantitative information provided from frequency scan fits to develop a method for quantitative concentration measurements by measuring the lifetime before and after optical dissociation of FeB pairs as outlined above. Frequency scans were performed at the center of a high-contamination region (in area B of Fig. 5) and well outside the defect region. The emissions from a halogen lamp were then directed onto the sample to a spot size diameter of $\sim$1.5 cm to obtain a white light intensity of approximately 85 W/cm^2. Lagowski et al.[10] studied the dissociation process for various intensities and durations and found that for [Fe] between 8×10^8 and 10^{13} cm^{-3}, optical dissociation was complete within 15 s using a white light intensity of 10 W/cm^2. Based on these results it was expected that the illumination used in the current experiments was sufficient for complete dissociation. A fan was used to move air across the sample surface during illumination to decrease any heating that may occur. The frequency scans were then repeated at the same location. The frequency scans and the fitting results are shown in Fig. 7. The recombination lifetime increased following dissociation, as expected for injection levels typical of PCR measurements.[7,47] The injection levels were calculated and used to determine the value of C for a

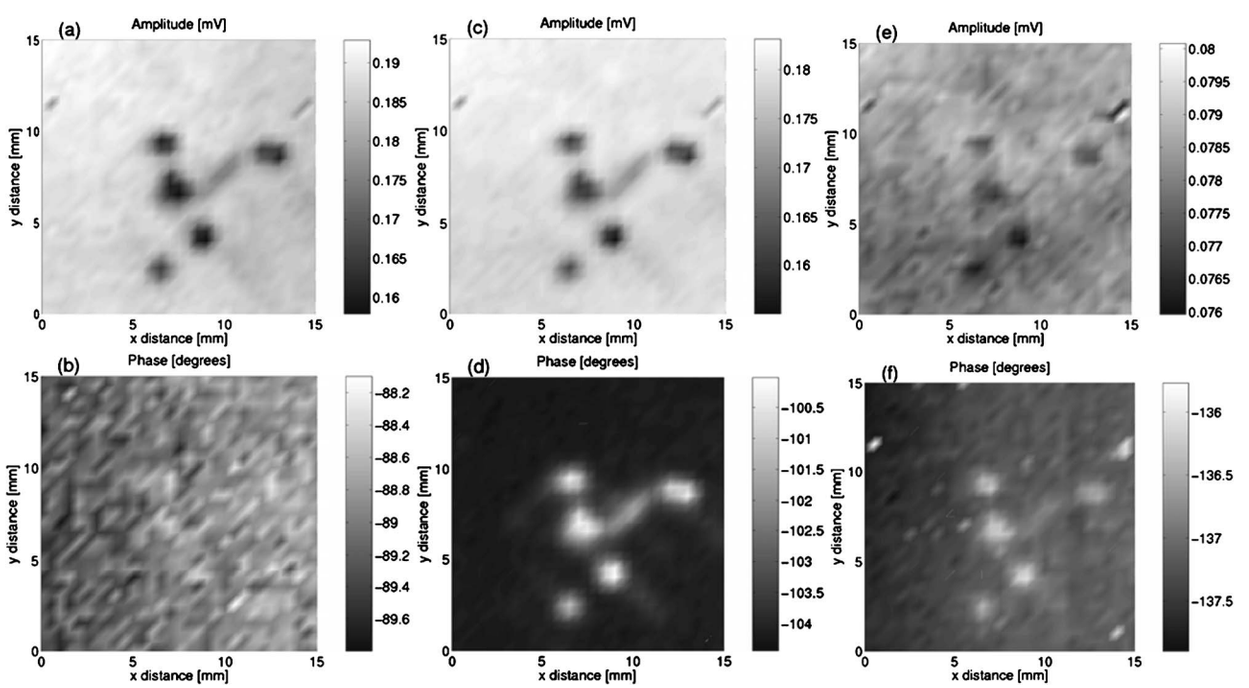

Figure 6. Amplitude and phase images of an Fe-contaminated wafer performed at modulation frequencies of 500 Hz (a & b), 6.5 kHz (c & d), and 100 kHz (e & f) with a step size of 0.5 mm.

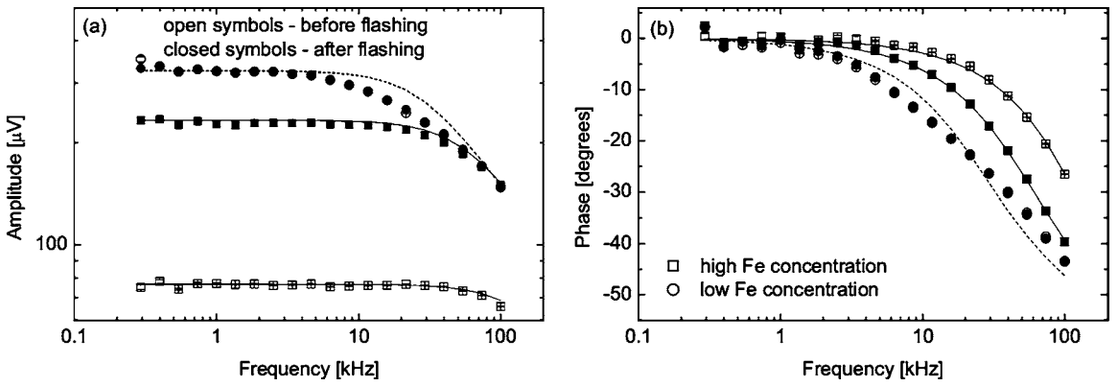

Figure 7. Frequency scans in regions of high and low iron concentration before and after flashing with white light. Recombination lifetime and resulting iron concentration calculations are presented in Table I.

doping density of 10^{15} cm^{-3} using Eq. 5, which was in turn used to determine the iron concentration from Eq. 4. The results of the calculations are shown in Table I.

The defect region with the lower PCR amplitude before flashing shows lower lifetimes and higher iron concentrations, as expected from the SPV results. The results for the region outside the defect clearly show that the overall amplitude and the frequency dependencies of the PCR signal remain relatively unaffected by white light illumination when compared to the scans performed in the highly contaminated region, and thus will have a much lower Fe concentration. However, the fitting to the theory is relatively poor for the low-[Fe] scans, most likely due to the inhomogeneous depth distribution of defects/contaminants in the near-surface region. The calculated iron concentrations in the low-lifetime regions were larger than the maximum value obtained from the SPV testing results. Outside of the highly contaminated region the calculated concentrations were within the range of the SPV measurements given for the entire wafer but still greater than expected. There are several potential reasons for the discrepancies. One factor is the higher spatial resolution of PCR. As the volume probed contracts about a defect cluster the relative contribution of the contaminant-related defect states becomes increasingly significant in the overall recombination statistics of excess carriers and, thus, the measured effective lifetime decreases accordingly. Another factor is the use of a single-level SRH theory to calculate the value of the prefactor C, as discussed earlier. For the injection levels used in these calculations, the use of the FeB acceptor level results in a value of C that is less than an order of magnitude greater than that obtained using the donor level. Finally, the sensitivity of the transport parameters to excess carrier density, and thus modulation frequency, along with the nonhomogeneous nature of the defect structure are likely to decrease the accuracy of the measured lifetimes and consequently the calculated iron concentration. The accuracy of the lifetime measurements could be improved significantly (to within ±20%) if the system could be operated at injection levels sufficiently low for the carrier diffusivity to be assumed constant.[49]

Table I. Lifetimes and iron concentration parameters calculated for the frequency scans presented in Fig. 7.

	High concentration		Low concentration	
Flashing state	Before	After	Before	After
Lifetime (μs)	0.8	3.0	6.4	6.5
Average injection level (cm^{-3})	2.46×10^{15}		6.05×10^{15}	
$1/C$ (s cm^{-3})	-1.13×10^{-8}		-1.46×10^{-8}	
PCR [Fe] (cm^{-3})	8.2×10^{13}		5.7×10^{10}	
Approx. SPV [Fe] (cm^{-3})	$>1.1 \times 10^{11}$		1.7×10^{10}	

It was suspected that the relatively high laser intensities used for PCR might be separating the iron–boron pairs during the exploratory imaging process required to locate the defect as well as during the frequency scans. This phenomenon has been noted previously when attempting to determine iron concentration using μ-PCD lifetime measurements.[47] μ-PCD utilizes injection levels that are similar to PCR and are many orders of magnitude greater than SPV requirements. To investigate this hypothesis the contaminated region in area B of Fig. 5 was located through PCR imaging and the sample was covered while still in the sample holder so that the defect would not have to be repositioned. The association time for FeB pairs has been shown to follow the relation[50]

$$\tau_{\text{pair}} \approx \frac{557T}{D_{\text{Fe}}N_A} \qquad [7]$$

where N_A is the acceptor (boron) concentration in cm^{-3}, T is the temperature in K, and D_{Fe_i} is the iron diffusivity in cm^2/s and can be calculated from[38]

$$D_{\text{Fe}_i} = 1.0 \times 10^{-3} e^{0.67\ \text{eV}/k_B T} \qquad [8]$$

The diffusion coefficient at room temperature is 3.094×10^{-15} cm^2/s and can be inserted into Eq. 7 with a doping density of 10^{15} cm^{-3} to calculate the association time constant of ~11.8 h. The sample was kept in the dark for approximately 36 h, which ensures that the majority of the iron should be in the FeB state, and the PCR signal at 10 kHz was then measured using a 300-μs lock-in time constant and a large beam size (935 μm radius) to minimize the laser intensity. The resulting signal transients are shown in Fig. 8. A rapid increase in the PCR amplitude within the first several minutes of exposure to the laser beam is observed. After 10 min the sample was moved so that the same time scan could be repeated outside the defective region. No transient due to laser–sample interaction was present in this low-iron-concentration area.

The signal transient, which is associated with FeB pair dissociation, is problematic for the conventional methodology of performing frequency scans via lock-in demodulation because the scans typically take approximately 10–15 min to perform due to the 1-s settling time of the lock-in amplifier to achieve acceptable signal-to-noise ratios. In addition, the sample is exposed to the excitation source during the imaging process required to locate the feature of interest prior to performing any frequency scans. Thus, a significant amount of FeB pairs are separated prior to, or in the early stages of, the frequency scan, resulting in underestimated iron concentration calculations. To reduce the overall exposure of the sample to laser beam illumination, a dynamic signal analyzer was used in place of the lock-in amplifier. The analyzer allowed frequency scans with 15 data points from 1 to 100 kHz to be performed in 21.2 s using a settling time of 100 ms and an integration time of 1.3 s. Attempts to

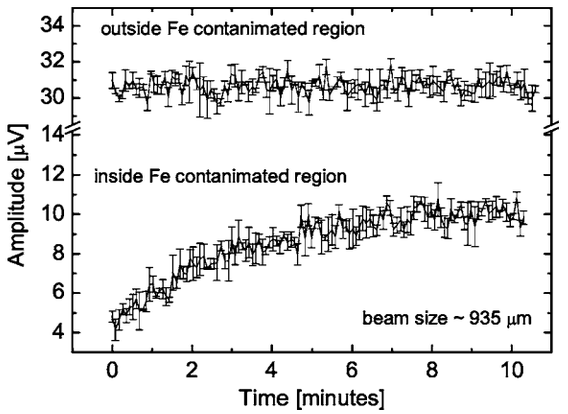

Figure 8. Signal transients due to separation of FeB pair by the excitation laser.

decrease either the settling time or the integration time resulted in frequency scans that were too noisy to be considered reliable and would not be able to provide accurate measurements when fitted to the theoretical model. The signal transient was sufficiently strong to have a significant influence on even these short 20-s frequency scans and prevented any fitting to theory for parameter extraction.

Conclusions

The ability to image the relative concentration of electronic defects and heavy-ion contaminants in Si wafers using photocarrier radiometry was demonstrated. The amplitude and phase of the PCR signal provide two independent channels for imaging and the contrast of each channel depends on the modulation frequency of the excitation source. A method for complete quantitative lifetime and/or subsurface depth imaging was developed through the combination of multifrequency images and/or frequency scans. Fe-contaminated wafers were successfully imaged and concentrations as low as 10^{11} cm^{-3} on a baseline of $\sim 5 \times 10^{9}$ cm^{-3} were easily distinguished. The resolution of PCR was shown to be superior to that of SPV due to the almost micrometer size of the excitation laser beam. The calculated iron concentration differed by up to approximately two orders of magnitude from the SPV results, likely due to the difference in the spatial resolution of the two techniques and the accuracy of the calculated recombination lifetimes from the PCR frequency scans. The attempts at quantitative measurement of iron concentration were also complicated by optical dissociation of the iron boron complex by the excitation laser. Attempts to resolve this problem using lower laser powers and the implementation of frequency-sweep waveforms allowing rapid ($\sim$20 s) frequency scans proved to be inadequate. Lower laser intensities (injection levels) during exposure to the laser beam will be required to improve the accuracy of iron concentration measurements using PCR.

Acknowledgments

Financial support of the Natural Sciences and Engineering Research Council of Canada (NSERC) and Materials and Manufacturing Ontario (MMO) through a Collaborative Contract are gratefully acknowledged. The authors thank Dr. Kirk Michaelian and Craig Hyett for performing the FTIR measurements at the Canadian Light Source in Saskatoon. The support of Analog Devices, Ireland, through the supply of Fe-contaminated wafers and SPV maps, is acknowledged.

References

1. C. J. Powell and M. P. Seah, *J. Vac. Sci. Technol. A*, **8**, 735 (1990).
2. S. J. B. Reed, *Electron Microprobe Analysis*, Cambridge University Press, New York (1993).
3. E. Chason, S. T. Picraux, J. M. Poate, J. O. Borland, M. I. Current, T. Diaz de la Rubia, D. J. Eaglesham, O. W. Holland, M. E. Law, C. W. Magee, J. W. Mayer, J. Melngailis, and A. F. Tasch, *J. Appl. Phys.*, **81**, 6514 (1997).
4. R. Klockenkamper, J. Knoth, A. Prange, and H. Schwenke, *Anal. Chem.*, **64**, 1115A (1992).
5. W. Shockley and W. T. Read, Jr., *Phys. Rev.*, **87**, 832 (1952).
6. R. N. Hall, *Phys. Rev.*, **87**, 387 (1952).
7. G. Zoth, in Recombination Lifetime Measurements in Silicon, ASTM STP 1340, D. C. Gupta, F. R. Bacher, and W. M. Hughes, Editors, p. 30, American Society for Testing Materials, Philadelphia, PA (1998).
8. D. K. Schroder, *Semiconductor Material and Device Characterization*, 2nd ed., Chap. 7, Wiley, New York (1998).
9. G. Zoth and W. Bergholz, *J. Appl. Phys.*, **67**, 6764 (1990).
10. J. Lagowski, P. Edelman, A. M. Kontkiewicz, O. Milic, W. Henley, M. Dexter, L. Jastrzebski, and A. M. Hoff, *Appl. Phys. Lett.*, **63**, 3043 (1993).
11. W. B. Henley, D. A. Ramappa, and L. Jastrezbski, *Appl. Phys. Lett.*, **74**, 278 (1999).
12. M. Tajima, *Appl. Phys. Lett.*, **32**, 719 (1978).
13. Y. Kitagawara, R. Hoshi, and T. Takenaka, *J. Electrochem. Soc.*, **139**, 2277 (1992).
14. O. King and D. G. Hall, *Phys. Rev. B*, **50**, 10661 (1994).
15. S. Pizzini, M. Guzzi, and G. Borionetti, *J. Phys.: Condens. Matter*, **12**, 10131 (2000).
16. J. R. Haynes and W. C. Westphal, *Phys. Rev.*, **101**, 1676 (1956).
17. Y. Hayamizu, R. Hoshi, Y. Kitagawara, and T. Takenaka, *Proc. SPIE*, **2638**, 113 (1995).
18. F. Kirscht, B. Orschel, V. Higgs, and A. Buczkowski, *Solid State Phenom.*, **69–70**, 259 (1999).
19. M. Acciarri, C. Cirelli, S. Pizzini, S. Binetti, A. Castaldini, and A. Cavallini, *J. Phys.: Condens. Matter*, **14**, 13223 (2002).
20. D. Guidotti, J. S. Batchelder, J. A. Van Vechten, and A. Finkel, *Appl. Phys. Lett.*, **48**, 68 (1986).
21. D. Guidotti, J. S. Batchelder, A. Finkel, P. D. Gerber, and J. A. Van Vetchen, *J. Appl. Phys.*, **66**, 2542 (1989).
22. R. K. Ahrenkiel, *Solid-State Electron.*, **35**, 239 (1992).
23. S. K. Krawczyk, M. Bejar, M. F. Nuban, R. C. Blanchet, A. Kostka, W. Warta, and J. P. Poly, *Inst. Phys. Conf. Ser.*, **160**, 1553 (1997).
24. A. Mandelis, J. Batista, and D. Shaughnessy, *Phys. Rev. B*, **67**, 205208 (2003).
25. A. Mandelis, *Solid-State Electron.*, **42**, 1 (1998); M. E. Rodriguez, A. Mandelis, G. Pan, L. Nicolaides, J. A. Garcia, and Y. Riopel, *J. Electrochem. Soc.*, **147**, 687 (2000).
26. J. Batista, A. Mandelis, and D. Shaughnessy, *Appl. Phys. Lett.*, **82**, 4077 (2003).
27. A. Mandelis, M. Pawlak, C. Wang, I. Delagadillo-Holfort, and J. Pelzl, *J. Appl. Phys.*, **98**, 123518 (2005).
28. D. Guidotti, J. S. Batchelder, A. Finkel, and J. A. Van Vechten, *Phys. Rev. B*, **38**, 1569 (1988-I).
29. A. Mandelis, *J. Appl. Phys.*, **97**, 083508 (2005).
30. B. Li, D. Shaughnessy, and A. Mandelis, *Rev. Sci. Instrum.*, **76**, 063703 (2005).
31. C.-M. Li, T. Sjodin, and H.-L. Dai, *Phys. Rev. B*, **56**, 15252 (1997).
32. V. Higgs, F. Chin, and X. Wang, *Solid State Phenom.*, **63–64**, 421 (1998).
33. A. Mandelis, *Diffusion-Wave Fields: Mathematical Methods and Green Functions*, Chap. 9, Springer, New York (2001).
34. M. Koizuka and H. Yamada-Kaneta, *J. Appl. Phys.*, **84**, 4255 (1998).
35. J. M. Hwang and D. K. Schroder, *J. Appl. Phys.*, **59**, 2476 (1986).
36. A. Borghesi, B. Pivac, A. Sassella, and A. Stella, *J. Appl. Phys.*, **77**, 4169 (1995).
37. S. M. Hu, *J. Appl. Phys.*, **51**, 5945 (1980).
38. A. A. Istratov, H. Hieslmair, and E. R. Weber, *Appl. Phys. A: Mater. Sci. Process.*, **69**, 13 (1999).
39. H. Feichtinger, *Inst. Phys. Conf. Ser.*, **46**, 528 (1979).
40. K. Graff and H. Pieper, *J. Electrochem. Soc.*, **128**, 669 (1981).
41. Y. Hayamizu, T. Hamaguchi, S. Ushio, T. Abe, and F. Shimura, *J. Appl. Phys.*, **69**, 3077 (1991); D. Walz, J.-P. Joly, and G. Kamarinos, *Appl. Phys. A: Mater. Sci. Process.*, **62**, 345 (1996).
42. C. B. Collins and R. O. Carlson, *Phys. Rev.*, **108**, 1409 (1957).
43. A. A. Istratov, H. Hieslmair, and E. R. Weber, *Appl. Phys. A: Mater. Sci. Process.*, **70**, 489 (2000).
44. L. Jastrzebski, J. Lagowski, W. Henley, and P. Edelman, in *Beam-Solid Interactions for Materials Synthesis and Characterization*, D. C. Jacobsen, D. E. Luzzi, T. F. Heinz, and M. Iwaki, Editors, p. 405, Materials Research Society, Pittsburgh, PA (1995).
45. J. Lagowski and P. Edelman, in *High Purity Silicon IV*, C. L. Claeys, P. Stallhofer, P. Rai-Choudhury, and J. E. Maurtis, Editors, p. 523, The Electrochemical Society Proceedings Series, Pennington, NJ (1996).
46. S. C. Choo, *Phys. Rev. B*, **1**, 687 (1970).
47. T. Pavelka, in Recombination Lifetime Measurements in Silicon, ASTM STP 1340, D. C. Gupta, F. R. Bacher, and W. M. Hughes, Editors, p. 206, American Society for Testing Materials, Philadelphia, PA (1998).
48. D. Macdonald, A. Cuevas, and J. Wong-Leung, *J. Appl. Phys.*, **89**, 7932 (2001).
49. B. Li, D. Shaughnessy, and A. Mandelis, *J. Appl. Phys.*, **97**, 023701 (2005).
50. L. C. Kimerling and J. L. Benton, *Physica B & C*, **116**, 297 (1983).